# Oscillations of Leading-Edge Vortex Breakdown Locations over a Delta Wing

Lu Shen* and Chih-yung Wen†

*Hong Kong Polytechnic University, Hong Kong, People's Republic of China*

**This paper presents an experimental investigation of the oscillations of the leading-edge vortex breakdown locations over a slender delta wing with a 75 deg sweep angle. Here, a new mechanism is proposed, the vortex–secondary-flow interaction, responsible for the quasi-periodic antisymmetric interaction of the leading-edge vortex breakdown locations; the induced secondary flow in the symmetric plane continuously transfers the disturbance induced by the leading-edge vortex breakdown from one semispan to another, as well as the corresponding positive feedback. Therefore, the oscillations of the leading-edge vortex breakdown locations are synchronized in an opposite phase by the induced secondary flow. The experimental results are consistent with this interaction mechanism. Moreover, a new small-scale oscillation of the leading-edge vortex breakdown location is observed upon the application of an improved peak-valley-counting method. Its frequency is in the range of the helical mode instability.**

## Nomenclature

| | | |
|---|---|---|
| $c$ | = | chord |
| $f$ | = | frequency |
| $Re$ | = | Reynolds number |
| $r$ | = | correlation coefficient |
| $t$ | = | time |
| $U_\infty$ | = | freestream velocity |
| $x, y, z$ | = | body coordinate |
| $x'$ | = | fluctuating value |
| $\bar{x}$ | = | mean value |
| $\alpha$ | = | angle of attack |

## I. Introduction

THE delta wing platform is a popular aircraft configuration because of its relatively high stall angle and good maneuverability. The dominant flow structure over a delta wing is a pair of counter-rotating leading-edge vortices (LEVs) that generate additional vortex lift and enhance stability and maneuverability. At a sufficiently high $\alpha$, the breakdown locations cross the trailing edge of the delta wing and move to the leeward side surface, resulting in a decrease in the vortex lift and an increase in the instability. In the past decades, a considerable amount of effort was dedicated to the study of the vortex breakdown theories [1–4]. Observations indicate that the quasi-periodic oscillations of the LEV breakdown locations are antisymmetric [5,6]. Gursul [7] suggested that a crossflow instability and a streamwise instability are responsible for the interaction of the LEV breakdown locations. However, the involvement of these two mechanisms lacks direct experimental evidence, and the underlying mechanism is still unclear.

To enrich our understanding of the oscillations of the LEV breakdown locations over slender delta wings, we conducted an experimental investigation in a low-speed wind tunnel. Flow visualization techniques and particle image velocimetry (PIV) were used to illustrate the LEV structure. By applying an improved peak-valley-counting (PVC) method, we obtained the probable frequencies of the small-scale oscillations of the LEV breakdown location. Here, we propose a new mechanism that is responsible for the interaction of the oscillations of the LEV breakdown locations: the vortex–secondary-flow interaction. The explanation of this mechanism is in good agreement with the experiment results. Meanwhile, a new small-scale oscillation of the LEV breakdown locations was identified, with its frequency in the range of the helical mode instability.

*Ph.D. Candidate, Department of Mechanical Engineering; lu.shen@connect.polyu.hk. Student Member AIAA.

†Professor, Department of Mechanical Engineering; cywen@polyu.edu.hk. Associate Fellow AIAA (Corresponding Author).

## II. Experimental Setup

The experiment was conducted in a closed-circuit wind tunnel with a test section of 60 cm (width) × 60 cm (height) × 240 cm (length). The delta wing model, shown in Fig. 1a, was made of aluminum, with a chord length of $c = 280$ mm, a sweep angle of 75 deg, and a thickness of 5 mm. The leading edges at the windward side were beveled at 35 deg to fix the separation point, which made the delta wing insensitive to Reynolds number [8]. The model was painted flat black to reduce laser reflection. The freestream velocity in the experiment ranged from 2.64 to 5.28 m/s, corresponding to Reynolds numbers ranging from 50,000 to 100,000 on the basis of the chord length. The angles of attack were set in the poststall region to ensure the LEV breakdown occurred on the upper surface of the delta wing. The freestream turbulence intensity was less than 0.5% in these cases. At a slip angle of 0 deg, the uncertainty between the central line of the delta wing and the wind tunnel was less than 0.1 deg.

In the flow visualization experiment, the flowfield was illuminated by a continuous laser (APGL-FN-532-1W). A high-speed camera (Photron FASTCAM SA-Z) and a normal digital camera (Nikon D5200) were used in the experiment. The Photron camera was used for continuous high-speed imaging at a high frame rate of 500 Hz and a resolution of 1000 × 1024 pixels. The Nikon camera was used to take snapshots with a resolution of 4000 × 6000 pixels and for recording videos at a frame rate of 50 Hz and a resolution of 720 × 1280 pixels. Two methods were used to generate smoke to visualize the flow structure. In the first method, a thin Cr-Ni wire with a diameter of 0.2 mm was vertically set at a distance of almost one chord length upstream of the delta wing apex. Olive oil droplets slipped down the wire smoothly because of gravity. A high concentration of smoke was generated continuously when the wire was heated by a dc power supply. In the preseeded flow visualization method, the entire wind tunnel was uniformly seeded with olive oil particles produced by a TSI 9307-6 aerosol generator. During the experiment, the oil particle density concentration in the wind tunnel was approximately 650 $\mu g/m^3$; thus, the overall flow density change was $(\rho' - \rho)/\rho < 0.1\%$. In the PIV measurements, a dual-pulse laser (with each pulse around 600 mJ) was used as the light source, and the images are acquired by a high-speed camera (HiSense 4M) with a resolution of 2048 × 2048 pixels. The TSI 9307-6 aerosol generator was also used for the PIV seeding. The analysis was performed

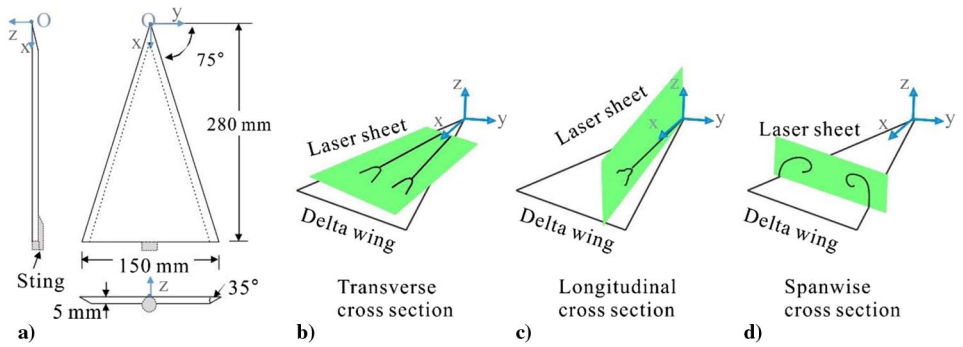


**Fig. 1 Schematics of a) the delta wing model, and b–d) the flow visualization setup for transverse cross section (Fig. 1b), longitudinal cross section (Fig. 1c), and spanwise cross section (Fig. 1d).**

using DynamicStudio with the adaptive correlation method. The arrangements of the delta wing model and the laser sheet are shown in Figs. 1b–1d. For the transverse cross section, the laser sheet crossed both cores of the LEVs and the camera recorded the observations from the top. For the longitudinal cross section, the laser sheet was perpendicular to the delta wing and crossed the LEV on one side, and the camera recorded the observations from the corresponding side. For the spanwise cross section, the laser sheet was placed spanwise and perpendicular to the delta wing, and the camera recorded the observations from the rear.

## III. Results and Discussion

### A. Flow Visualization

The results of the smoke flow visualization and the preseeded flow visualization in the transverse cross section are shown in Figs. 2a and 2b, respectively. They were recorded by the digital camera. In general, when the laser sheet flow visualization technology is used, the vortex core structure is often depicted as a "black hole" in the radial cross section or a "black line" in the axial cross section and the sudden expansion of the vortex core structure is regarded as the location of the vortex breakdown [9–11]. In Fig. 2a, the entire LEV structure is occupied by highly concentrated smoke. In the center of each LEV, the black line (marked by white arrows) indicates the LEV cores. At around $x = 0.7c$ (marked by dashed white circles), the black lines suddenly expanded and then disappeared, implying the LEV breakdown. In Fig. 2b, the LEV cores and the LEV breakdown locations are also clearly illustrated by the preseeded flow visualization. Similar results shown in Fig. 2a and 2b revealed that this preseeded method was reliable for the laser sheet flow visualization technique. Moreover, this preseeded method could provide a considerably more detailed LEV structure with appropriate processing, as demonstrated in Fig. 2c. The original frame was captured by the digital camera during the preseeded flow visualization. The brightness and contrast of the frame were adjusted to highlight the detailed structure. Besides the core and its breakdown, the tiny vortical substructures in the shear layer could also be easily identified. Therefore, this method achieved a good balance between the global flow evolution and the local small structures. Thus, it is a promising flow visualization method for investigating the vortical flow.

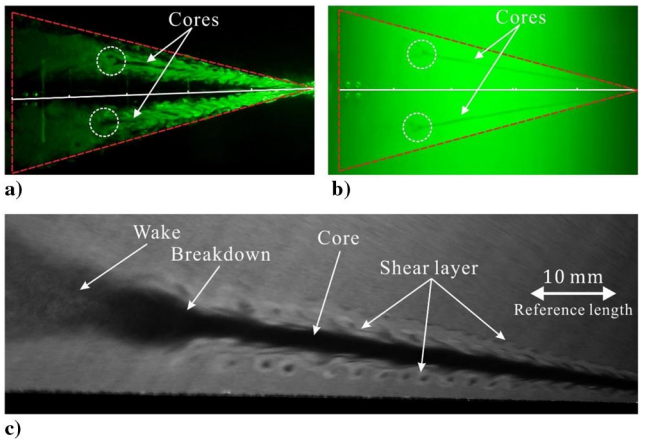


**Fig. 2 a–b) Flow visualizations in the transverse cross section: $\alpha = 36$ deg; $Re = 50{,}000$, c) processed grayscale frame showing the LEV structure in the longitudinal cross section: $\alpha = 44$ deg; $Re = 100{,}000$.**

The identification and the measurement of the LEV breakdown location were based on the images acquired in the preseeded flow visualization experiments. A MATLAB code was developed to process the images and measure the LEV breakdown location. Figure 3a presents an example captured by the high-speed camera. During the experiment, the LEV breakdown location always fluctuated in the dashed square region. Thus, this region was extracted for processing. The noise caused by the laser reflection and the nonuniform distribution of the laser sheet strength was removed, and the grayscale image was transformed into a binary image, as shown in Fig. 3b. The next step was to sum up the values in each column of the binary image and plot them as Fig. 3c. A significant structure expansion is usually observed when a vortex breakdown occurs. Therefore, a sudden change in the slope of the summation was used as the criterion for the vortex breakdown location. The measurement uncertainty of the LEV breakdown location in this case was less than $0.001c$. During the experiments, both bubble-type and spiral-type vortex breakdowns were observed. Nevertheless, the breakdown type did not influence the breakdown position measurement.

### B. Breakdown Locations Oscillation

Figure 4a shows the typical time history of the LEV breakdown location in the case of $\alpha = 44$ deg and $Re = 50{,}000$. It was measured from the frames taken by the high-speed camera at a sampling frequency of 500 Hz, corresponding to a time resolution of $\Delta t = 0.019c/U_\infty$. The total recording duration was $t \approx 190c/U_\infty$ (only part of the time history is shown in Fig. 4a). The centerline $x'/c = 0$ denotes the time-averaged breakdown location. The positive $x'/c$ indicates the downstream, and the negative $x'/c$ represents the upstream. Both small-amplitude oscillations and large-amplitude oscillations were clearly observed in the time history. Figure 4e shows the corresponding power spectrum of the oscillations of the LEV breakdown location. The peak at $fc/U_\infty = 0.11$ represents the dominant large-amplitude oscillation of the LEV breakdown location. This dimensionless frequency is consistent with that found in other previous works [6,12,13].

However, small-scale oscillations were not observed in the power spectrum shown in Fig. 4e because of their small amplitude. To estimate the corresponding frequency band of these small-scale oscillations, a peak-valley-counting (PVC) technique [14] was used. Unlike Menke et al. [5], we improved the PVC method by taking the peak-to-valley value of the oscillations into consideration during the pairing up. Thus, the improved PVC method could avoid the missing

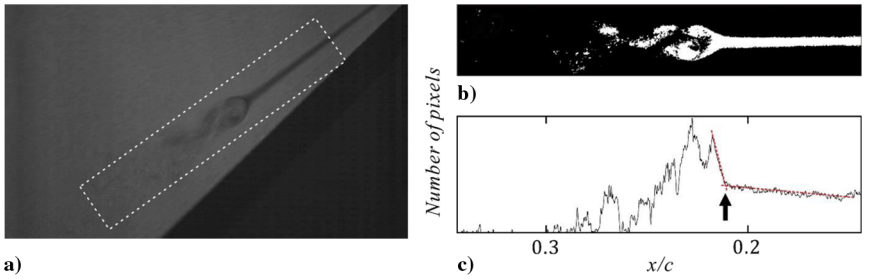


**Fig. 3 a) Preseeded flow visualization in the longitudinal cross section: $\alpha = 44$ deg, $Re = 50{,}000$; b) the processed binary image; and c) the summation of each column in the binary image.**

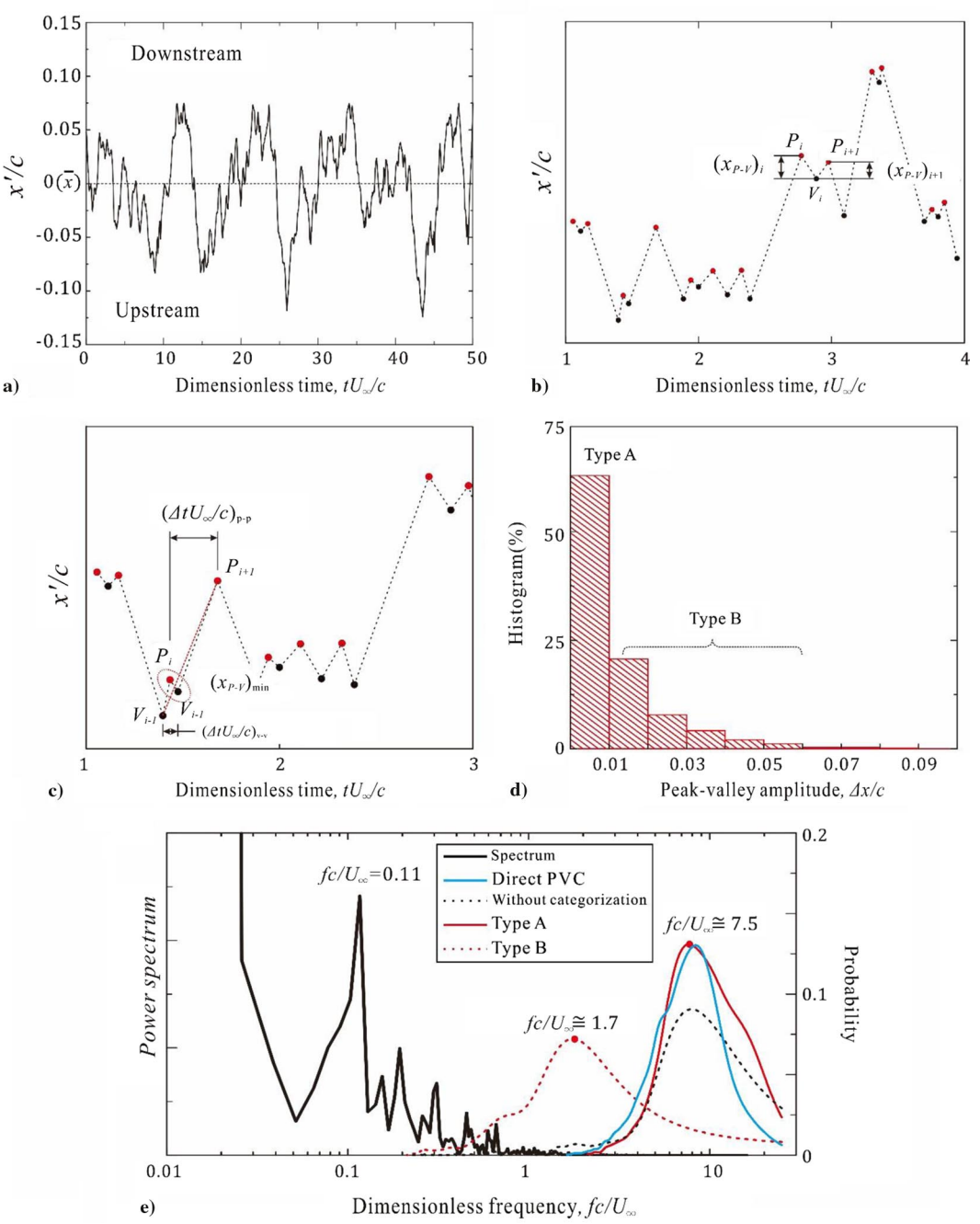


**Fig. 4 a) A time history of the LEV breakdown location: $\alpha = 44$ deg, $Re = 50{,}000$; b–d) the improved PVC processing; and e) the power spectrum and the probability densities.**

of long-period oscillations (which might have been divided into several short-period oscillations if the original PVC method was used). The steps are as follows.

1) Locate local peaks and valleys in the time history of the oscillation of the LEV breakdown location and create a new time history with only these peaks and valleys (see Fig. 4b).

2) Calculate the distance between the neighboring peaks and valleys, $x_{P-V} = (x_P - x_V)$ (see Fig. 4b).

3) Find the minimum $x_{P-V}$, and pair up the corresponding peak $P_i$ and valley $V_i$ (see Fig. 4c).

4) Compute the interval time between peak $P_i$ and $P_{i+1}$, $\Delta(tU_\infty/c)_{P-P}$, as well as that between valley $V_i$ and $V_{i-1}$, $\Delta(tU_\infty/c)_{V-V}$ (see Fig. 4c). Assume the smaller one of these two interval times to be the period of this oscillation.

5) As in the case shown in Fig. 4c, $\Delta(tU_\infty/c)_{V-V}$ denotes the period of this local small oscillation. Therefore, calculate the amplitude of this oscillation $\Delta x$ as the mean value of the distances of $V_{i-1}$ to $P_i$ and $P_i$ to $V_i$.

6) Remove the peak $P_i$ and valley $V_i$ from the time history shown in Fig. 4c.

7) Repeat steps 2–6 until all peaks and valley are paired up.

The frequency spectrum of the local small-scale oscillations was predicted by using the corresponding period from the time history [15].

The statistics of the amplitudes of the successfully paired-up peak valleys are shown in Fig. 4d. This histogram shows that the amplitudes of the small-scale oscillations varied in a wide range. Thus, they were categorized into two types on the basis of their amplitude: type A (63.2% of the total pairs) with an amplitude of $\Delta x/c \leq 0.01$, and type B (36.8%) with an amplitude of $0.01 < \Delta x/c$. The longer-period larger-amplitude oscillations were preserved by this improved PVC method and were decomposed from the shorter-period smaller-amplitude ones. The corresponding frequency probabilities of these small-scale oscillations are shown in Fig. 4c. This figure clearly shows that these two types of small-scale oscillations were in two different frequency bands. Type A (the smaller-scale) oscillations were in the higher-frequency band ($(fc/U_\infty)_{\text{peak}} \cong 7.5$) and in the same range as the Kelvin–Helmholtz instability. For type B oscillations, the frequency band ($(fc/U_\infty)_{\text{peak}} \cong 1.7$) was almost in the same range as the helical mode instability detected in the LEV breakdown wake [7,8]. This frequency band embedded in the oscillation of the LEV breakdown location was observed for the first time ever, in this study. Therefore, we hypothesized that this small-scale oscillation of the LEV breakdown location was strongly related to the helical mode instability in the wake. However, whether this small-scale oscillation of the LEV breakdown location promotes the helical mode instability or is its byproduct is still unknown.

The result of the frequency probability obtained by the aforementioned improved PVC method but without any categorizations of the oscillations is shown in Fig. 4e with the black dotted line. For comparison, the result obtained using the same PVC method as that in [5] is also shown in Fig. 4e with the blue line. These two probability distributions were almost in the same frequency band, which was in the same range as the Kelvin–Helmholtz instability in the rolling-up shear layer from the leading edges [16,17]. These probability distributions of the small-scale oscillations were very similar to the result reported by Menke et al. [5].

The breakdown locations of both LEVs were recorded simultaneously in the transverse cross section by the digital camera from the top of the wind tunnel. The corresponding time resolution was $\Delta t = 0.19c/U_\infty$, and the recording duration was $t \approx 1100c/U_\infty$. Thus, the highest frequency oscillation (type A) was not detected in these cases. Because the amplitude of type A oscillation was very small, the result was hardly affected by the absence of type A oscillations. Figure 5a shows the time histories of both the LEV breakdown locations in the case with $\alpha = 40$ deg and $Re = 50{,}000$. The oscillations of these breakdown locations were almost opposite to each other. The corresponding correlation coefficient between these time histories was $r = -0.53$, indicating a strong antisymmetric interaction between the oscillations on the starboard side and the port side. The dominant oscillations were around $fc/U_\infty \cong 0.093$, as shown in Fig. 5b. These results were consistent with those reported by Menke and Gursul [18]. The improved PVC method was also applied to decompose small-scale oscillations on the starboard side and the port side. The peaks of both the probability densities were in the band of $fc/U_\infty = 1.4$–$1.8$, as shown in Fig. 5b.

Later, a splitter plate was installed in the symmetric plane of the delta wing for the comparison with the aforementioned baseline case. The splitter plate was placed in the symmetric plane from the apex of the delta wing to $0.1c$ after the trailing edge. The thickness of the plate was $0.007c$ and its height was $0.357c$, which was sufficient high to stop any crossflow interaction between the two semispans [19]. The leading edge of the plate was beveled at 75 deg to match the delta wing geometry. The time histories of both LEV breakdown locations are plotted in Fig. 5c. The correlation coefficient between these two time histories was $r = 0.04$, which revealed that the LEV breakdown locations were independent of each other. Unmistakably, the antisymmetric motion of the LEV breakdown locations was suspended by the splitter plate. Meanwhile, the amplitude of the breakdown location oscillations decreased obviously, as indicated by the reduction of the standard deviation, from $x'_{\text{rms}}/c = 0.028$ and 0.029 (port and starboard, respectively) to $x'_{\text{rms}}/c = 0.020$ and 0.020,

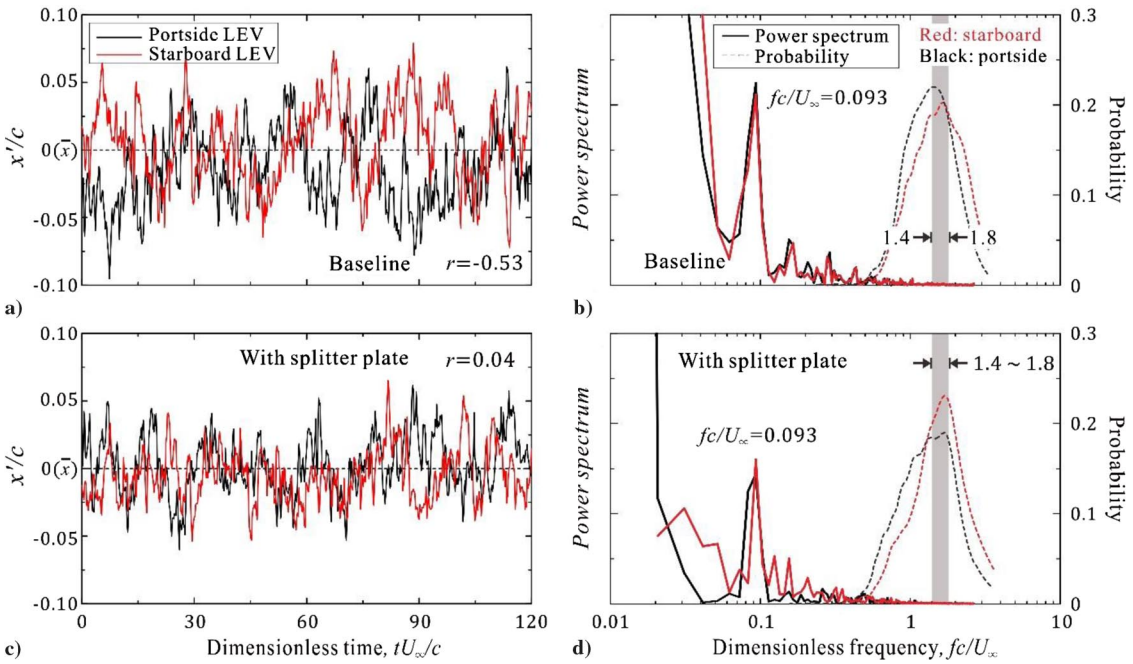


**Fig. 5 a) and c) Time histories of the LEV breakdown locations; b) and d) the corresponding power spectrums and the probability densities: $\alpha = 40$ deg, $Re = 50{,}000$.**

with a decrease of approximately 30%. Moreover, the LEV cores were slightly shifted to the outboard side in the spanwise direction because of the splitter plate. However, the structures before the breakdown locations remained stationary; in Fig. 5d, the frequency spectrum peaks of the dominant oscillations were located at $fc/U_\infty \cong 0.093$, the same as those in the baseline case. The PVC analysis clearly showed that the probability densities of the small-scale oscillations also remained in the same band as those in the baseline case. Therefore, the unsteady oscillation of the LEV breakdown location is known as a result of the local semispan flow structure. Summarily, in the baseline case, the interaction between the LEV breakdown locations played the role of a synchronizer to correlate the dominant oscillations at each semispan in their natural frequency band with an almost opposite phase. The larger amplitude of the oscillations in the baseline case than that in the splitter plate case was attributed to the resonance at the dominant frequency.

### C. Vortex–Secondary-Flow Interaction

To further understand the interaction between the LEV breakdown locations, the flow structures in the spanwise cross section were investigated via PIV measurements. As shown in Figs. 5a–5c, the observation was in the perpendicular plane at $x = 0.4c$, with $\alpha = 40$ deg and $Re = 100{,}000$. This location was close to the time-averaged LEV breakdown locations of both sides. Therefore, flow structures with the stable LEV core and LEV breakdown could be obtained. The time-averaged vorticity contours shown in Fig. 6a indicated that strong shear layers rolled up from the leading edges and wrapped into the central large-scale vortex core. From the instantaneous snapshots shown in Figs. 6b and 6c, because of the Kelvin–Helmholtz instability, small-scale vortices were shed from the leading edge, moved up along the curved shear layer, and finally fed into the primary vortex core. The pairing of these small-scale vortices was also often observed during the smoke flow visualization (Fig. 2c). The streamlines in the time-averaged result clearly showed a saddle point and a half-saddle point in the symmetric plane. The overall flow structures were time-averaged symmetric. However, the instantaneous snapshots revealed that the flow structures were asymmetric and alternated from time to time. In Fig. 6b, the broken core vorticity concentrations on the starboard side revealed that the LEV breakdown on this semispan had already occurred in the upstream flowfield and led to an expansion of the local flow structure. The outer flow around the broken LEV followed this expansion and became divergent, instead of rolling into the center. Topologically, the streamlines on the starboard side formed an unstable spiral. On the port side, a relatively concentrated vorticity contour was visible, indicating the LEV core. Moreover, the streamlines illustrated a topology of a stable focus. Note that the red instantaneous streamline traveled from the starboard side to the port side, crossing the symmetric plane. In Fig. 6c, the flowfield was in the opposite condition: on the starboard side, the streamlines exhibited a stable focus; and on the port side, the structure was an unstable spiral. The induced secondary flow moved from the port side to the starboard side. These two typical instantaneous flow structures suggested that the interaction of the LEV breakdown locations was related to the induced secondary flow in the symmetric plane.

Here, we propose that a new mechanism, the vortex–secondary-flow interaction, is responsible for the antisymmetric interaction of the LEV breakdown locations. In this mechanism, the streamwise self-oscillation of the LEV breakdown locations is a necessary part of the onset of the antisymmetric interaction. Once a vortex breakdown occurs in the upstream field and its location moves forward, for example, on the starboard side in Fig. 6d, the flow structure becomes asymmetric in the spanwise (as shown in Fig. 6b); a part of the rolling-up flow on the starboard side crosses the symmetric plane and merges into the portside flow (marked by the red dot line in Fig. 6d). The occurrence location of this induced spanwise secondary flow, called the inflection point, moves forward with the starboard LEV breakdown location. This leads to a reduction of the crossflow area on the port side and a slight increase in the momentum. Therefore, a contraction effect is induced on the port side. Earlier studies on a single vortex [20,21] have reported that the contraction can significantly affect the entire flowfield and benefit a delay of the vortex breakdown location, whereas a divergence of the stream tube can cause the vortex breakdown [22]. In this scenario, the LEV breakdown location on the port side is delayed downstream, following the same tendency as its natural motion; meanwhile, the induced secondary flow in the downstream alternates to the port side, leading to an area expansion on the starboard side, which further promotes the advance of the LEV breakdown location on the starboard side. Because the LEV breakdown locations are inherently self-oscillatory, they soon reach their extreme upstream or downstream positions and switch their own motions. Now, imagine the LEV breakdown location on the starboard side is moving downstream, as shown in Fig. 6e. The inflection point also moves downstream, leading to an expansion of the flow structure on the port side before the vortex breakdown. This enhances the advancing motion of LEV breakdown location on the port side. Simultaneously, the LEV breakdown on the port side pushes the induced secondary flow to the starboard and results in a contraction on the starboard side. This continuously excites the delaying motion of the LEV breakdown location on the starboard side. Once the LEV breakdown locations

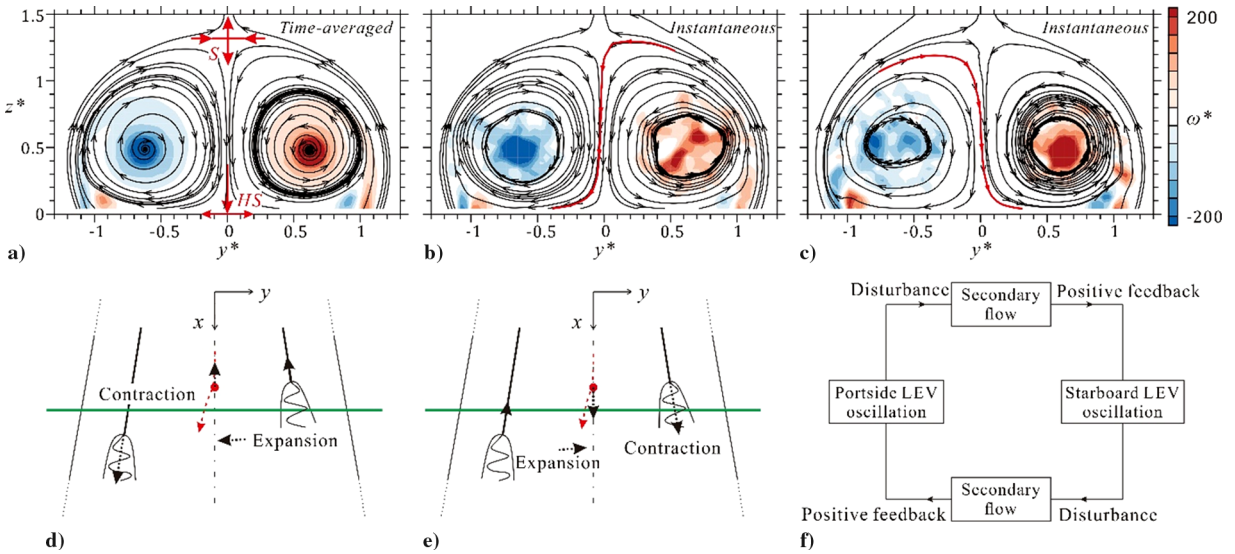


**Fig. 6 a–c) Vorticity contour and streamlines in the crossflow perpendicular plane with $x = 0.4c$, $\alpha = 40$ deg, and $Re = 100{,}000$; d–e) interactions between the LEV breakdown locations; and f) the vortex-secondary-flow interaction.**

cross their mean position, the quasi-periodic antisymmetric interaction switches to the opposite phase (see in Fig. 6c) and continues as that discussed in the earlier half-cycle.

In summary, in the vortex–secondary-flow interaction, the two self-oscillatory LEV breakdown locations and the secondary flow form a positive feedback closed loop, as shown in Fig. 6f. The oscillations of the LEV breakdown locations generate disturbances, which are propagated from one semispan to another through the induced secondary flow in the symmetric plane and considerably enhance the motions of the LEV breakdown locations. Simultaneously, the enhanced oscillation of the LEV breakdown location enlarges its disturbance and transfers it to the other semispan as a positive feedback. Because of this vortex–secondary-flow interaction, the oscillations of the LEV breakdown locations are synchronized in the opposite phase, and the amplitude of these oscillations is amplified. The result presented in the previous section agreed well with this mechanism.

## IV. Conclusions

An experimental investigation was conducted to study the quasi-periodic antisymmetric oscillations of the leading-edge vortex (LEV) breakdown locations over a slender delta wing. It was shown that the vortex–secondary-flow interaction was responsible for the antisymmetric oscillations of the LEV breakdown locations on a slender delta wing. The induced secondary flow between the pair of LEVs transferred the disturbance, induced by the LEV breakdowns, from one semispan to another. This enhanced the natural motions of the LEV breakdown locations and induced positive feedback, which also went through the induced secondary flow. Therefore, the phases of the oscillations were synchronized. With a splitter plate in the symmetric plane, the correlated motions of LEV breakdown locations were suspended, and the amplitude of the oscillations was significantly suppressed. Meanwhile, the frequencies of the oscillations were rarely affected. The experimental results showed a good agreement with the proposed mechanism. In addition, an improved PVC method was applied to decompose the oscillations from the time history of the LEV breakdown locations. For the first time, a small-scale oscillation was observed at a frequency in the range of the helical mode instability.

## Acknowledgments

The authors would like to thank Hong Kong Research Grants Council (number GRF526913), Hong Kong Innovation and Technology Commission (number ITS/334/15FP), and the U.S. Office of Naval Research Global (monitored by Woei-min Lin, number N00014-16-1-2161) for financial support.

## References

[1] Leibovich, S., "The Structure of Vortex Breakdown," *Annual Review of Fluid Mechanics*, Vol. 10, 1978, pp. 221–246. doi:10.1146/annurev.fl.10.010178.001253

[2] Benjamin, T. B., "Some Developments in the Theory of Vortex Breakdown," *Journal of Fluid Mechanics*, Vol. 28, No. 01, 1967, pp. 65–84. doi:10.1017/S0022112067001909

[3] Delery, J. M., "Aspects of Vortex Breakdown," *Progress in Aerospace Sciences*, Vol. 30, No. 1, 1994, pp. 1–59. doi:10.1016/0376-0421(94)90002-7

[4] Lucca-Negro, O., and O'Doherty, T., "Vortex Breakdown: A Review," *Progress in Energy and Combustion Science*, Vol. 27, No. 4, 2001, pp. 431–481. doi:10.1016/S0360-1285(00)00022-8

[5] Menke, M., Yang, H., and Gursul, I., "Experiments on the Unsteady Nature of Vortex Breakdown over Delta Wings," *Experiments in Fluids*, Vol. 27, No. 3, 1999, pp. 262–272. doi:10.1007/s003480050351

[6] Mitchell, A. M., Barberis, D., Molton, P., and Délery, J., "Oscillation of Vortex Breakdown Location and Blowing Control of Time-Averaged Location," *AIAA Journal*, Vol. 38, No. 5, 2000, pp. 793–803. doi:10.2514/2.1059

[7] Gursul, I., "Review of Unsteady Vortex Flows over Slender Delta Wings," *Journal of Aircraft*, Vol. 42, No. 2, 2005, pp. 299–319. doi:10.2514/1.5269

[8] Breitsamter, C., "Unsteady Flow Phenomena Associated with Leading-Edge Vortices," *Progress in Aerospace Sciences*, Vol. 44, No. 1, 2008, pp. 48–65. doi:10.1016/j.paerosci.2007.10.002

[9] Payne, F. M., Ng, T., Nelson, R. C., and Schiff, L. B., "Visualization and Wake Surveys of Vortical Flow over a Delta Wing," *AIAA Journal*, Vol. 26, No. 2, 1988, pp. 137–143. doi:10.2514/3.9864

[10] Shen, L., Wen, C.-y., and Chen, H.-A., "Asymmetric Flow Control on a Delta Wing with Dielectric Barrier Discharge Actuators," *AIAA Journal*, Vol. 54, No. 2, 2016, pp. 652–658. doi:10.2514/1.J054373

[11] Nelson, R. C., and Pelletier, A., "The Unsteady Aerodynamics of Slender Wings and Aircraft Undergoing Large Amplitude Maneuvers," *Progress in Aerospace Sciences*, Vol. 39, No. 2, 2003, pp. 185–248. doi:10.1016/S0376-0421(02)00088-X

[12] Gursul, I., and Yang, H., "On Fluctuations of Vortex Breakdown Location," *Physics of Fluids*, Vol. 7, No. 1, 1995, pp. 229–231. doi:10.1063/1.868724

[13] Lambert, C., and Gursul, I., "Insensitivity of Unsteady Vortex Interactions to Reynolds Number," *AIAA Journal*, Vol. 38, No. 5, 2000, pp. 937–939. doi:10.2514/2.1053

[14] Huang, L.-S., and Ho, C.-M., "Small-Scale Transition in a Plane Mixing Layer," *Journal of Fluid Mechanics*, Vol. 210, Jan. 1990, pp. 475–500. doi:10.1017/S0022112090001379

[15] Prasad, A., and Williamson, C. H. K., "The Instability of the Shear Layer Separating from a Bluff Body," *Journal of Fluid Mechanics*, Vol. 333, Feb. 1997, pp. 375–402. doi:10.1017/S0022112096004326

[16] Gad-El-Hak, M., and Blackwelder, R. F., "The Discrete Vortices from a Delta Wing," *AIAA Journal*, Vol. 23, No. 6, 1985, pp. 961–962. doi:10.2514/3.9016

[17] Riley, A. J., and Lowson, M. V., "Development of a Three-Dimensional Free Shear Layer," *Journal of Fluid Mechanics*, Vol. 369, Aug. 1998, pp. 49–89.

[18] Menke, M., and Gursul, I., "Unsteady Nature of Leading Edge Vortices," *Physics of Fluids*, Vol. 9, No. 10, 1997, pp. 2960–2966. doi:10.1063/1.869407

[19] Cai, J., Luo, S., and Liu, F., "Stability of Symmetric and Asymmetric Vortex Pairs over Slender Conical Wings and Bodies," *Physics of Fluids*, Vol. 16, No. 2, 2004, pp. 424–432. doi:10.1063/1.1637601

[20] Escudier, M., Bornstein, J., and Zehnder, N., "Observations and LDA Measurements of Confined Turbulent Vortex Flow," *Journal of Fluid Mechanics*, Vol. 98, No. 1, 1980, pp. 49–63. doi:10.1017/S0022112080000031

[21] Chao, Y., Leu, J., Hung, Y., and Lin, C., "Downstream Boundary Effects on the Spectral Characteristics of a Swirling Flowfield," *Experiments in Fluids*, Vol. 10, No. 6, 1991, pp. 341–348. doi:10.1007/BF00190250

[22] Hall, M. G., "Vortex Breakdown," *Annual Review of Fluid Mechanics*, Vol. 4, 1972, pp. 195–218. doi:10.1146/annurev.fl.04.010172.001211